energies

MDPI

Article

Flying Car Battery Pack Design Based on Tortoise Carapace Bionic Casing and Metamaterial Sandwich Core

Ying Zhao [1,*], Kaiming Chen [1], Xiaoyu Sun [1], Boheng Zhao [1], Jibo Hao [2], Yueqiang Wang [3] and Yangwei Wang [4]

[1] College of Engineering and Technology, Southwest University, Chongqing 400715, China; ckm20040612@email.swu.edu.cn (K.C.); 13541603361@163.com (X.S.); zbh612@email.swu.edu.cn (B.Z.)
[2] College of Automotive Engineering, Jilin University, Changchun 130025, China; haojb25@mails.jlu.edu.cn
[3] School of Automation, Chongqing University, Chongqing 401331, China; 202513257677@stu.cqu.edu.cn
[4] National Key Laboratory of Science and Technology on Materials Under Shock and Impact, Beijing Institute of Technology, Beijing 100081, China; wangyangwei@bit.edu.cn
* Correspondence: zy2019@swu.edu.cn

Abstract

To provide reliable impact protection for a flying car power battery pack under stringent lightweight requirements, especially under takeoff, landing, and drop impact scenarios, a biomimetic metamaterial sandwich enclosure inspired by the hierarchical protective architecture of a tortoise carapace is proposed. The enclosure is composed of an outer shell, an internal sandwich core, and an inner plate, through which load diffusion and deformation buffering can be achieved by multilayer structural coordination. Firstly, three core configurations, including conventional honeycomb, a chiral structure with negative Poisson's ratio (NPR) characteristics, and an NPR concave structure, are comparatively investigated through high-speed impact finite element simulations. The NPR concave structure is regarded as the preferred core configuration due to its more balanced energy absorption behavior and superior deformation stability. Afterwards, the NPR concave structure is embedded into the full battery pack enclosure, and the protective performances of the proposed battery pack are evaluated under representative flying car operating conditions. Compared with those of the conventional honeycomb, the maximum displacement of the proposed battery pack decreases by 49.31% under the takeoff-and-landing overload condition, and the maximum intrusion decreases by 25.94% under the drop impact condition. The results indicate that the tortoise-carapace-inspired metamaterial sandwich structure effectively enhances the deformation resistance and anti-intrusion capability of a flying car battery pack, thereby providing a feasible structural design approach for battery protection in flying car applications.

Keywords: flying car; battery pack; tortoise-shell-inspired design; metamaterial sandwich core; negative Poisson's ratio structure

Check for updates

Academic Editors: Junfeng Liu and Ka Wai Eric Cheng

Received: 20 June 2026
Revised: 15 July 2026
Accepted: 17 July 2026
Published: 21 July 2026

Copyright: © 2026 by the authors. Licensee MDPI, Basel, Switzerland. This article is an open access article distributed under the terms and conditions of the Creative Commons Attribution (CC BY) license.

1. Introduction

With the ongoing transition of global energy structure and the decarbonization of transportation systems, electrification, intelligent mobility, and three-dimensional transportation have attracted increasing attention. These trends are regarded as key development directions for future transportation equipment under carbon-neutrality-oriented strategies. Electric flying cars integrate the functions of both ground vehicles and low-altitude aircraft. Owing to this dual-mode mobility, the spatial constraints of traditional road networks can

be partially alleviated. As an important component of future integrated transportation systems, safety, reliability, and overall performance of electric flying cars have become critical issues in current research and engineering design [1,2]. Different from conventional ground electric vehicles, flying cars must satisfy both lightweight flight requirements and structural safety requirements under complex operating conditions. Therefore, the protection performance of the onboard power battery pack is directly related to the safety and reliability of whole vehicle.

For flying cars, the power system serves as the foundation of overall performance. As the core energy storage component, power battery directly determines the endurance capability, power output, and center-of-gravity distribution of the vehicle, and is closely associated with operational safety [3,4]. Compared with traditional ground electric vehicles, flying car battery packs are subjected to be much harsher and more complex service environments.

On the one hand, flying cars are required to operate in multiple modes, including vertical takeoff and landing, hovering, cruising, and ground driving. These diverse operating modes impose stringent requirements on overall mass, thrust-to-weight ratio, and energy efficiency. Therefore, the battery pack structure should be designed to be as lightweight as possible while still providing sufficient protection, thereby reducing energy consumption and extending flight endurance. On the other hand, flying cars are subjected to complex mechanical loads during operation, such as landing impact, vertical drop, and lateral collision. Once a battery pack experiences severe impact or compression, internal cells may undergo structural failure, short circuit, electrolyte leakage, or even thermal runaway, which will result in serious safety accidents [3,5]. Therefore, improving impact resistance, anti-intrusion capability, and energy absorption performance of a power battery pack under strict mass constraints remains a critical issue in flying car structural design.

Relevant experience can be drawn from battery protection and rollover safety studies for ground vehicles. Existing research has examined battery pack enclosures, side and bottom impact protection, local reinforcement, and energy-absorbing components. These studies show that enclosure stiffness, structural layout, and module protection strongly affect crashworthiness and battery safety. Rollover performance has also been investigated under established regulatory frameworks. UN/ECE Regulation No. 66 specifies structural strength and residual space requirements for large passenger vehicles [6]. Based on this regulation, Karliński et al. [7] evaluated bus superstructures using finite element analysis, while Liang and Le [8] investigated rollover protection with LS-DYNA. Kunakorn-ong and Jongpradist [9] further optimized bus super-structures by considering both rollover crashworthiness and lightweight design. For electric vehicles, UN/ECE Regulation No. 100 defines safety requirements for electric powertrains and rechargeable electrical energy storage systems (REESS) [10]. A recent study combining ECE R66 and ECE R100 showed that battery pack layout, mounting, structural integrity, and deformation control strongly influence intrusion risk and battery safety during electric bus rollover [11]. These studies provide a useful basis for battery system protection. However, they mainly address buses and conventional road vehicles. Flying car battery packs experience additional load paths, including vertical overload during takeoff and landing and high-speed drop impact. Their protection performance therefore requires dedicated assessment under flight-specific conditions.

Current protective designs for power battery packs still rely heavily on traditional aluminum alloy plates and conventional honeycomb sandwich structures [12,13]. However, under the stringent lightweight constraints of flying car design, conventional battery pack structures struggle to achieve a favorable balance between impact resistance and energy absorption under extreme crash conditions. To overcome this limitation, biomimetic

structural design has emerged as a promising approach for lightweight protection [14,15]. Through millions of years of natural selection, a wide range of biological topologies with lightweight characteristics and excellent mechanical properties has evolved in nature. These natural structures provide valuable inspiration for engineering protection design. For instance, bamboo achieves lightweight characteristics and high bending resistance through the gradient distribution of fiber bundles [16]. Similarly, nacre can significantly improve resistance to crack propagation through its brick-and-mortar layered architecture [17]. From the perspective of geometric evolution and performance improvement, the formation of hierarchical architectures in natural systems can also be interpreted through constructal design theory. Constructal law describes how finite-size flow systems with freedom to change configuration tend to evolve toward architectures that facilitate access to internal currents [18–20]. Although this law does not prescribe specific protective geometries, it provides a physical framework for linking geometric evolution, transport pathways, and system performance. In structural protection, this framework helps explain how hierarchical architectures improve load transfer, stress redistribution, and energy dissipation.

Similar to these natural systems, the tortoise carapace represents a typical biological protective structure. It consists of a hard outer scute, a porous middle bony layer, and an internal supporting framework. Through this hierarchical sandwich configuration, impact loads can be diffused, local deformation can be accommodated, and energy can be dissipated via multilevel structural synergy. As a result, excellent stress dispersion and energy absorption capabilities can be achieved by the tortoise carapace [21,22]. From the perspective of structural mechanics, the power battery pack also functions as a system composed of an outer load-bearing enclosure and internal sensitive cells. Its protection requirements are highly consistent with the mechanical characteristics of the tortoise carapace. Therefore, introducing the macroscopic layered protection mechanism of the tortoise carapace into battery pack design can effectively optimize the impact load transmission path. This strategy can also alleviate local stress concentration and exhibits considerable potential for lightweight protective engineering. However, most existing biomimetic protection studies focus on the direct abstraction of biological shell features or the design of individual protective components. The coordinated design of biomimetic load-bearing enclosures and architected energy-absorbing cores for battery pack protection remains insufficiently explored.

However, the protection challenges faced by a flying car battery pack under extreme conditions cannot be fully addressed by macroscopic biomimetic shell alone, and an internal sandwich core is still required for effective energy dissipation. With the development of complex topological design methods, mechanical metamaterials have demonstrated significant advantages in crash energy absorption, as their mechanical responses can be tailored through microstructural geometry [23,24]. When metamaterials are employed as the sandwich core of battery pack, the energy dissipation capability within the biomimetic shell can be further enhanced. Compared with conventional honeycombs, metamaterials such as negative Poisson's ratio (NPR) structures and chiral structures exhibit unique local densification and contraction mechanisms under compression, thereby providing higher specific stiffness, specific energy absorption, and intrusion resistance [25]. In recent studies, NPR metamaterials have also been applied to vehicle crash beams, energy-absorbing boxes, and power battery pack protective structures, and their superior potential over traditional honeycomb materials in improving crashworthiness and energy absorption has been confirmed [26,27]. However, most existing studies assess metamaterial cores at unit-cell or component scale. Interactions among metamaterial sandwich cores, biomimetic enclosures, internal battery modules, and connection regions within complete battery pack systems remain insufficiently understood. Moreover, trade-offs among energy absorption,

peak load control, crushing stability, and pack-level deformation resistance have not been systematically investigated.

In summary, macroscopic shell design and microscopic sandwich core optimization are generally treated as two separate domains in current research on power battery pack protection. Although load transmission paths can be optimized through macroscopic biomimetic design, internal space utilization and energy dissipation efficiency remain limited. In contrast, microscopic metamaterials can provide outstanding specific energy absorption; however, an appropriate macroscopic load-bearing framework is still required to prevent overall structural instability under complex mechanical loading. At present, the synergistic integration of natural protective mechanisms and artificial metamaterials has rarely been investigated. Moreover, most existing studies focus mainly on conventional crash conditions for ground vehicles. Systematic comparison and evaluation of battery pack protection under the multidimensional and complex operating conditions unique to flying cars, such as vertical drop, takeoff impact, and landing impact, remain critically lacking [1,2,28].

To address the above research gaps, this paper proposes an integrated tortoise-carapace-inspired metamaterial sandwich design framework for the protection of flying car power battery packs. The proposed framework couples biological hierarchical protection with architected metamaterial energy absorption and pack-level crashworthiness evaluation. Inspired by the multilevel protective architecture of the tortoise carapace, the dense external scute, porous middle bony layer, and internal supporting structure are abstracted into a collaborative protection system composed of a load-bearing battery pack shell and an energy-absorbing metamaterial sandwich core. Through this biomimetic–metamaterial integration, load diffusion, deformation buffering, and energy dissipation are incorporated into a lightweight battery pack enclosure. Within this framework, three representative sandwich core topologies, including a conventional honeycomb, an NPR chiral structure, and an NPR concave structure, are developed and compared under consistent material, design space, and relative density conditions. High-speed impact simulations are conducted to systematically evaluate their deformation modes, energy absorption characteristics, peak load response, crushing stability, and intrusion resistance. This comparison enables the preferred sandwich core configuration to be selected based on a comprehensive balance among multiple crashworthiness indicators, rather than a single performance metric. Furthermore, the selected NPR concave core is introduced into the full battery pack enclosure to evaluate its protective performance at the pack level. This step extends the analysis from cellular core response to complete battery pack structural protection, where interactions among the biomimetic enclosure, metamaterial sandwich core, internal battery modules, and connection regions can be considered. Representative flying car operating conditions, including vertical overload during takeoff and landing and dynamic drop impact, are then investigated. Finite element simulations are performed for both the proposed biomimetic metamaterial battery pack and the conventional honeycomb-based structure. The results demonstrate that the proposed design effectively improves deformation resistance and anti-intrusion capability under lightweight constraints. Therefore, this study establishes a multiscale biomimetic–metamaterial design route for high-safety and lightweight battery pack protection in flying car applications.

2. Structural Design and Modeling

Based on the hierarchical protective mechanism of a tortoise carapace, a biomimetic sandwich structure is proposed for the flying car battery pack. As described in Figure 1, the microsection of a tortoise carapace is geometrically abstracted, and its heterogeneous structure is simplified into three macroscopic regions: a dense outer shell, a porous sandwich

core, and a solid supporting layer. In this study, the upper and lower shells of the battery pack are designed independently according to the proposed biomimetic configuration. Specifically, both shells consist of an outer cover, a cellular metamaterial sandwich core, and an inner plate, corresponding to the hierarchical features of the tortoise carapace. Through coordinated large-deformation behavior, the multilayer sandwich design enables load diffusion and energy dissipation, thereby protecting the internal cell module.

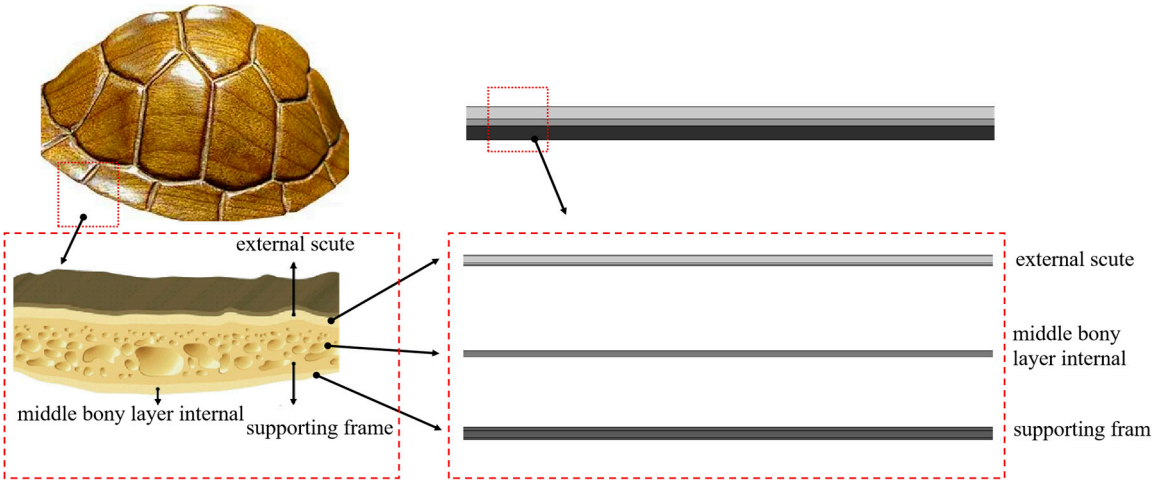


Figure 1. Hierarchical structure and geometric abstraction of tortoise carapace cross section.

On this basis, according to the structural characteristics of a flying car power battery pack and the requirements for finite element simulation, geometric and finite element models of the power battery pack are established, as depicted in Figure 2. To improve computational efficiency, non-load-bearing accessories, including thermal management pipelines and electrical wiring harnesses, are excluded from the model. Owing to the complex combination of multilayer shells and solid structures in the overall system, hexahedral elements are primarily employed to discretize major components. Specifically, solid components, including shell, tray, and metamaterial core, are modeled using eight-node reduced-integration solid elements. The global base mesh size is set to 9 mm, and local mesh refinement is applied to contact regions where large deformation is likely to occur.

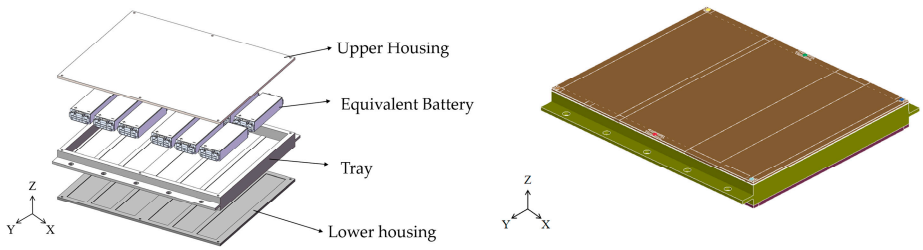


Figure 2. Three-dimensional geometry and finite element simulation model of the flying car power battery pack.

The internal battery modules are represented as equivalent crushable-foam blocks in the full-pack finite element model. This simplification is adopted because the present study focuses on the global deformation resistance and anti-intrusion performance of the battery pack enclosure, rather than on the detailed failure evolution of individual cells. Similar macromechanical equivalent modelling strategies have been widely used in mechanical simulations of lithium-ion batteries and battery modules to improve computational efficiency while retaining the main compression and crushing characteristics of the cell assembly [29,30]. In the present model, the equivalent crushable-foam material is used

to describe the macroscopic compressive stiffness, volumetric compaction, load-bearing response, and energy-dissipation tendency of the battery module under external mechanical loading. Therefore, the interaction between the enclosure and the internal battery modules can be considered at the pack level, and the intrusion response of the enclosure can be evaluated. However, the detailed internal structure of a real battery module is not explicitly resolved. Specifically, the layered electrode–separator structure, cell casing, tabs, busbars, inter-cell gaps, module frame, local cell-to-cell contact, local buckling of cell shells, electrochemical reactions, thermal effects, and short-circuit failure evolution are not included in the equivalent model. Therefore, the equivalent crushable-foam model is mainly used for pack-level structural protection evaluation, while detailed local cell failure and multiphysics safety behavior still require refined cell-level or module-level models.

Connections between components are defined according to actual assembly relationships. Bolted joints connecting upper shell, lower shell, and tray are represented using a simplified CBEAM–RBE2 coupling method. For each bolted joint, a CBEAM element is established along the nominal bolt axis to represent the axial, bending, and shear stiffness of the bolt shank. End nodes of the CBEAM element are coupled to surrounding nodes in corresponding bolt-hole regions through RBE2 elements. In this way, the main load-transfer path between bolt and connected plates is introduced into the full battery pack model. This simplified representation captures the primary load-transfer behavior of bolted joints while maintaining computational efficiency in pack-level simulations. Detailed joint features, including bolt threads, washer contact, bolt preload, hole clearance, and bearing contact between bolt shank and hole wall, are not explicitly modeled. Rigid kinematic coupling introduced by RBE2 elements may also restrict local deformation around bolt holes. Calculated peak stresses near bolted joints may therefore be affected by idealized connector stiffness. In this study, stress concentrations around bolted joints are used mainly to identify potential high-stress regions and load-transfer paths rather than to predict exact local stresses around real bolt holes. Meanwhile, the interface between metamaterial core and shell plates is defined using a shared-node connection. The final model contains 715,288 elements, with an average mesh quality of 0.918, satisfying mesh-quality requirements for subsequent simulations [31].

Material properties of major components are summarized in Table 1. Q235 steel is assigned to the upper shell, lower shell, and tray, while aluminum alloy is used for the metamaterial sandwich core; internal battery modules are represented by the equivalent crushable-foam model described above. Q235 steel and aluminum alloy are defined using rate-independent elastic–plastic constitutive models, and strain-rate dependence is not explicitly considered for either metallic components or equivalent battery material. Therefore, numerical results are mainly used to compare global deformation, load transfer, energy absorption, and intrusion resistance among different battery pack configurations under consistent material, boundary, and loading conditions, rather than to provide calibrated predictions of rate-dependent local failure or absolute peak stress.

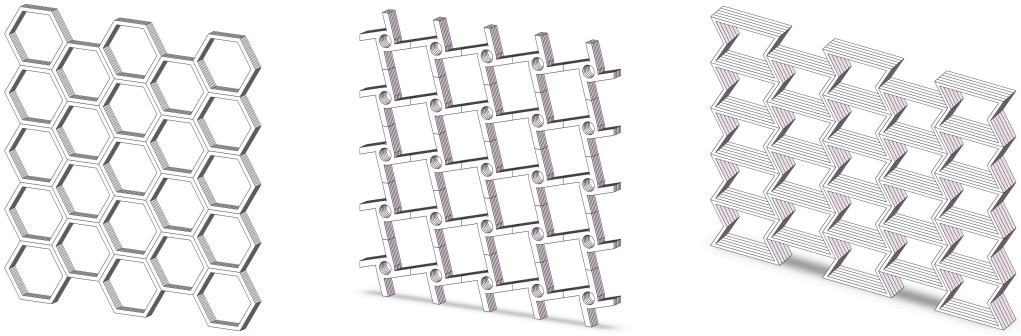
Table 1. Material properties of major components in a battery pack.

Component	Material	Density (g/cm^3)	Elastic Modulus (MPa)	Poisson's Ratio
Upper/lower shells and trays	Q235 steel	7.85	210,000	0.30
Battery modules	Equivalent battery material	2.20	800	0.35
Metamaterial sandwich substrates	Aluminum alloy	2.75	68,200	0.33

3. Metamaterial Design and Optimization

3.1. Metamaterial Configurations

Based on the biomimetic sandwich structure of a battery pack established in Section 2, several metamaterial configurations are introduced as alternative core units to further enhance the impact resistance and energy absorption capacity of sandwich layer in flying car power battery pack. For comparison, three cell topologies are considered, namely conventional honeycomb, NPR chiral structure, and NPR concave structure. Their geometric configurations are presented in Figure 3.



(**a**) (**b**) (**c**)

Figure 3. Unit cell geometric configurations of sandwich cores. (**a**) Conventional honeycomb. (**b**) NPR chiral structure. (**c**) NPR concave structure.

The three configurations shown in Figure 3 are developed as representative sandwich core topologies based on the concept of constructal design [18–20]. Constructal design provides a useful theoretical framework for relating geometric configuration to load-transfer paths, deformation modes, and structural performance. Guided by this concept, the conventional honeycomb, NPR chiral structure, and NPR concave structure are selected to represent different core architectures with distinct load-bearing and energy-absorbing mechanisms. Within this configuration-design framework, energy absorption, peak crushing force, deformation stability, and intrusion resistance are adopted as the main performance criteria. The present study compares these representative core topologies under controlled material and mass conditions, so that a suitable sandwich core configuration can be identified for subsequent full-pack protection analysis.

The conventional honeycomb is denoted in Figure 3a. As one of the most widely used lightweight sandwich core configurations in engineering applications, it is selected as the baseline configuration in the present work [32]. The structure consists of periodically arranged regular hexagonal unit cells in plane, providing high in-plane supporting stiffness and good manufacturability [33]. Its broad engineering applicability makes it a reliable benchmark for evaluating protective performance of other sandwich configurations.

The NPR chiral structure is illustrated in Figure 3b. It consists of circular nodes and tangentially connected ligaments, with rotatable nodes serving as the defining feature of the unit cell [34]. Under external compression, circular nodes rotate and induce coordinated bending and rotational deformation of the ligaments, thereby generating an overall contraction response [35]. This deformation mechanism differs markedly from those of the conventional honeycomb and NPR concave structure. Therefore, an NPR chiral structure is adopted as a representative topology for analyzing response characteristics of different NPR structures under varying loading conditions.

The NPR concave structure presented in Figure 3c represents a typical NPR topology derived from conventional honeycomb [36]. Unlike conventional honeycomb, an NPR concave structure features inward-recessed cell walls that form re-entrant unit cells with

concave angles. Under compressive loading, the recessed cell walls rotate, bend, and contract inward. As a result, the NPR effect is exhibited in the transverse direction [25]. This structure preserves the connectivity of a conventional honeycomb while exhibiting the contraction characteristics of an NPR structure. Therefore, it demonstrates strong potential for crushing stability, energy absorption efficiency, and intrusion resistance.

To ensure a fair comparison and address lightweight design requirements, all sandwich cores are assigned the same base material, with a density of 2750 kg/m^3, and occupy the same core design space. Relative densities are maintained at comparable levels as far as permitted by geometric differences, while core mass is calculated from solid volume in each finite element model. All components outside the sandwich core remain unchanged; therefore, differences in total battery pack mass arise only from core topology. Unit cell parameters, relative density, core mass, total pack mass, and normalized mass ratio of each configuration are summarized in Table 2. This controlled comparison allows differences in crashworthiness to be attributed mainly to topology-induced deformation and load-transfer mechanisms rather than additional material usage.

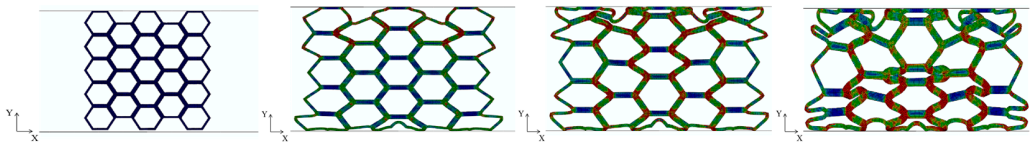
Table 2. Unit cell geometric parameters for three structures.

Structural Configuration	Relative Density	Unit Cell Width/mm	Unit Cell Height/mm
Conventional honeycomb	0.23	64.62	55.96
NPR chiral structure	0.23	43.16	43.16
NPR concave structure	0.23	32.36	21.36

3.2. Crashworthiness Under Drop Impact

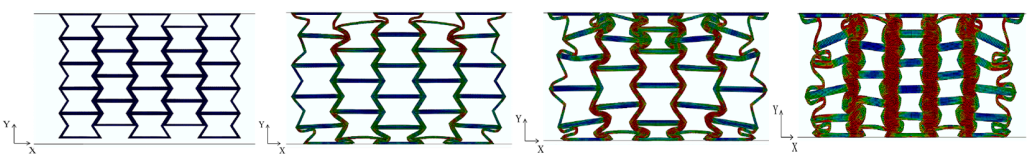
To evaluate the impact resistance of different metamaterial sandwich core configurations in the flying car battery pack and identify an optimal core configuration for subsequent full-pack design, impact finite element models of several sandwich arrays are established in Abaqus/Explicit. Each unit cell configuration is constructed as a 5 × 5 × 5 periodic array.

For the impact condition, a constant-strain scheme is adopted to accurately evaluate the impact resistance of each structure and minimize differences in energy absorption caused by structural characteristics. The impact velocity is fixed at 17.5 m/s, and the structural strain is set to 0.8. Subsequently, the specific energy absorption (SEA) and peak crushing force (PCF) after impact are analyzed. The deformation and stress contours of different sandwich structures at various strain levels are presented in Figures 4–6.



(**a**) (**b**) (**c**) (**d**)

Figure 4. Deformation modes of the conventional honeycomb under impact loading. (**a**) ε = 0. (**b**) ε = 0.20. (**c**) ε = 0.40. (**d**) ε = 0.60.



(**a**) (**b**) (**c**) (**d**)

Figure 5. Deformation modes of the NPR concave structure under impact loading. (**a**) ε = 0. (**b**) ε = 0.20. (**c**) ε = 0.40. (**d**) ε = 0.60.

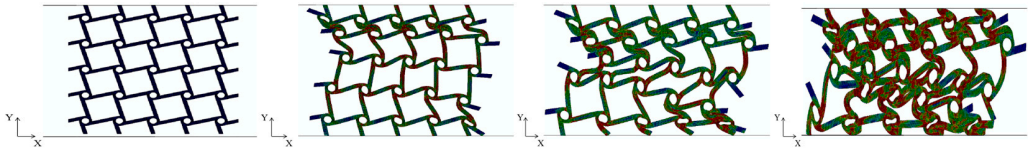


Figure 6. Deformation modes of the NPR chiral structure under impact loading. (**a**) $\varepsilon = 0$. (**b**) $\varepsilon = 0.20$. (**c**) $\varepsilon = 0.40$. (**d**) $\varepsilon = 0.60$.

The deformation characteristics shown in Figures 4–6 are generally consistent with experimental and numerical observations reported for honeycomb and auxetic cellular structures. Ruan et al. [37] investigated in-plane dynamic crushing of conventional honeycombs using ABAQUS and showed that impact velocity and cell wall thickness significantly affect localized deformation modes and plateau stress. These findings agree with the localized cell wall bending and progressive folding observed in Figure 4. For NPR concave structures, Dong et al. [38] compared finite element predictions with compression experiments and reported that deformation modes and crushing stresses approach experimental results when more than four cells are included in both transverse and longitudinal directions. Therefore, the $5 \times 5 \times 5$ periodic array adopted in this study provides a representative domain for evaluating the crushing response of the NPR concave core. Gao et al. [39] further confirmed that re-entrant auxetic structures exhibit inward contraction, progressive densification, and enhanced energy dissipation under dynamic compression, consistent with the response shown in Figure 5. For NPR chiral structures, Qi et al. [40] demonstrated that impact energy absorption is governed mainly by coupled node rotation and ligament bending, which agrees with the deformation pattern observed in Figure 6. Overall, the predicted deformation mechanisms agree well with published experimental and numerical observations. This agreement supports the credibility of the present finite element framework and provides a reasonable basis for the comparative assessment of the three sandwich core configurations.

The deformation modes indicate that conventional honeycomb mainly deforms through cell wall bending and local folding under impact loading. As depicted in Figure 4, crushing first occurs in the upper and lower regions near the loading plates. In these regions, the end cells are progressively flattened, whereas the middle cells still retain part of their hexagonal shape after impact. As this structure does not exhibit an obvious lateral contraction effect, impact energy is mainly dissipated through cell wall bending. As a result, its overall deformation coordination and sustained load-carrying capacity remain relatively limited.

The deformation behavior of the NPR concave structure under impact loading differs markedly from that of the conventional honeycomb. As described in Figure 5, this structure exhibits pronounced inward contraction during compression. The cell walls deform in a coordinated manner through rotation, bending, and inward shrinkage, indicating a typical NPR response. The cells near the upper and lower ends collapse first at the initial contact stage, whereas the central region also deforms simultaneously. As a result, more uniform compression is maintained and no obvious premature local instability is observed. These results indicate that the NPR concave structure exhibits good crushing stability and sustained load-carrying capability.

The deformation mode of the NPR chiral structure is mainly governed by the coupled effects of nodal rotation and ligament bending. As presented in Figure 6, pronounced rotation occurs in circular nodes after impact, inducing significant bending deformation of the connecting ligaments. As a result, the overall structure exhibits a tendency toward tilting and deflection. Although impact energy is dissipated through nodal rotation and

ligament deformation, local deformation is not fully uniform, and the overall crushing path remains relatively complex. Therefore, local regions are more prone to asymmetric deformation and stiffness degradation. Consequently, its crushing stability is lower than that of the NPR concave structure.

To further compare the impact protection performance of three sandwich configurations, the post-impact deformation contours alone cannot fully reflect the differences in load-bearing capacity and energy absorption during the entire impact process. Therefore, based on the deformation mode analysis above, the stress–strain data of each structure during impact are further extracted, and the corresponding SEA and PCF values listed in Table 3 are evaluated. The stress–strain curves are plotted in Figure 7. These results more clearly reveal the differences in overall crashworthiness of various metamaterial sandwich structures under dynamic impact.

Table 3. SEA and PCF of different structures.

Structural Configuration	SEA/kJ·g^{-1}	PCF/kN
Conventional honeycomb	0.56	57.73
NPR chiral structure	3.14	25.11
NPR concave structure	1.31	43.38

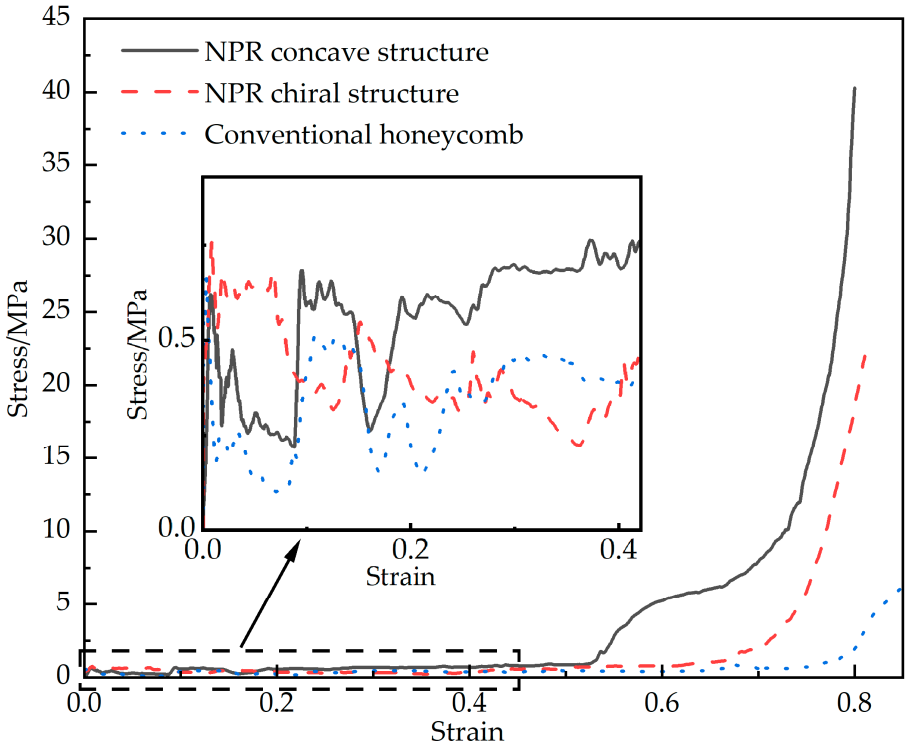


Figure 7. Stress–strain curves of three structures.

The results indicate that the conventional honeycomb delivers an SEA of only 0.56 kJ/kg, whereas the corresponding PCF reaches 57.73 kN. This result reveals poor mass-specific energy absorption and a high initial impact load. As denoted in Figure 7, the stress increases rapidly during compression, whereas the subsequent load-bearing plateau remains unstable. Therefore, conventional honeycomb exhibits difficulty in balancing load attenuation and sustained support. The NPR chiral structure achieves an SEA of 3.14 kJ/kg, indicating strong energy absorption per unit mass. However, its PCF still reaches 25.11 kN. As further depicted in Figure 7, considerable impact energy is absorbed by this structure through nodal rotation and ligament bending. Nevertheless, the stress–strain curve fluctuates markedly, indicating

limited overall stability. In contrast, the NPR concave structure exhibits an SEA of 1.31 kJ/kg. Although this value is lower than that of the NPR chiral structure, it is still significantly higher than that of the conventional honeycomb. Meanwhile, its PCF is only 43.38 kN, which is lower than that of the conventional honeycomb but higher than that of the NPR chiral structure. Figure 7 further demonstrates that the stress increases relatively slowly at the initial compression stage, thereby helping to reduce the instantaneous load at the onset of impact. As the strain increases, the stress then rises rapidly, indicating that the structure can still provide strong support after progressive densification. Based on the above comparison, the NPR concave structure is selected as the preferred sandwich core configuration for the flying car battery pack. At the unit cell scale, the NPR chiral structure achieves the highest SEA and the lowest PCF. However, its pronounced stress fluctuations and relatively complex deformation path indicate lower crushing stability. In comparison, the NPR concave structure provides moderate energy absorption, a lower PCF than the conventional honeycomb, and a more stable inward-contraction mode. These characteristics provide a better balance among energy absorption, peak load control, crushing stability, and deformation resistance. Because the primary design objective of this study is to reduce global displacement and intrusion at pack scale rather than to maximize SEA alone, the NPR concave structure is adopted for subsequent battery pack analyses.

4. Protection Performance Evaluation of Flying Car Battery Pack Under Typical Operating Conditions

Based on the above results, the NPR concave structure is selected as the optimal sandwich core for a flying car power battery pack. Its performance is subsequently compared with that of a conventional honeycomb under static takeoff-and-landing and dynamic drop conditions. Before finite element analysis is performed on battery packs with different core layers, material properties of each component should be defined. As an equivalent material modeling method is adopted in this study, equivalent elastic modulus and Poisson's ratio of different core structures are determined first. Structural parameter diagrams of the conventional honeycomb and the NPR concave structure is presented in Figure 8.

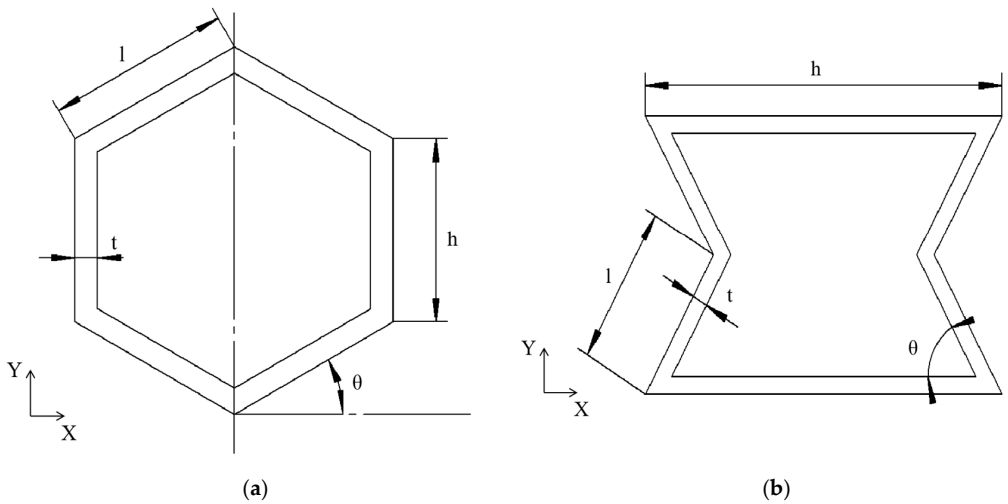


Figure 8. Structural parameters of the unit cell. (**a**) The unit cell of a conventional honeycomb. (**b**) The unit cell of an NPR concave structure.

For a conventional honeycomb, the equivalent elastic properties can be estimated using the elastic deformation model proposed by Masters and Evans [32]. For the NPR concave structure, the equivalent mechanical model is established based on Castiglioni's second theorem and Timoshenko beam theory [41]. In both models, the cell wall is idealized

as a slender beam, and the in-plane deformation of the structure is assumed to be governed mainly by cell-wall bending [32,41].

Under the assumptions of small deformation, linear elasticity, and thin-walled geometry, the equivalent Young's modulus and equivalent Poisson's ratio of the conventional honeycomb and NPR concave structure mainly depend on the following parameters: E_s represents the Young's modulus of the cell-wall base material; t is the cell-wall thickness; l refers to the length of the inclined cell wall; h gives the length of the vertical cell wall; and θ is the angle between the inclined cell wall and the horizontal axis in the theoretical model. Accordingly, the equivalent Young's modulus E^* and the equivalent Poisson's ratio ν^* can be expressed as follows:

$$E^* = E_s\left(\frac{t}{l}\right)^3 \frac{\left(\frac{h}{l} + \sin\theta\right)}{\cos^3\theta} \tag{1}$$

$$\nu^* = \frac{sin\theta\left(\frac{h}{l} + \sin\theta\right)}{\cos^2\theta} \tag{2}$$

Material and geometric parameters of the honeycomb used in this study are as follows: E_s = 70 GPa, t = 4 mm, l = 30 mm, h = 30 mm, and θ = 30°. Accordingly, the in-plane equivalent Young's modulus of the regular equilateral hexagonal honeycomb is calculated to be approximately E_A^* = 383 MPa, and its in-plane equivalent Poisson's ratio is ν_A^* = 1. It should be noted that this value is the equivalent Poisson's ratio derived from the geometric deformation mechanism, rather than the Poisson's ratio of the cell-wall base material. Therefore, the equivalent Poisson's ratio obtained from experiments or finite element simulations may differ from the theoretical value.

For the NPR concave structure, the material and geometric parameters are E_s = 70 GPa, t = 1.3 mm, l = 11.55 mm, h = 30 mm, and $\theta = -60°$. Accordingly, the in-plane equivalent Young's modulus of the NPR concave structure is calculated to be approximately E_B^* = 1582 MPa, and its in-plane equivalent Poisson's ratio is $\nu_B^* = -0.167$.

The equivalent Young's modulus and Poisson's ratio described above should be interpreted as small-strain, in-plane homogenized properties of the cellular cores. These parameters are used to define the initial elastic stiffness and in-plane deformation tendency of each core configuration. However, they are not sufficient to independently represent the nonlinear collapse, progressive crushing, and densification behavior of cellular structures under large deformation.

Therefore, in the full-pack LS-DYNA simulations, the explicit cellular geometry is not replaced by a purely linear elastic continuum. Instead, the sandwich core is represented as a homogenized crushable cellular material. The equivalent elastic parameters define only the initial small-strain response, whereas the subsequent compression and crushing behavior is governed by a tabulated macroscopic compressive response curve. For the NPR concave core adopted in the full-pack model, the corresponding response curve is shown in Figure 9. This curve describes the transition from the initial elastic stage to the plateau crushing stage dominated by progressive cell-wall collapse and finally to the densification stage. In this way, the main strain-dependent crushing characteristics of the cellular core are retained at the macroscopic level.

Since honeycomb and auxetic cellular structures generally exhibit anisotropic mechanical responses, the equivalent core properties are defined according to the dominant load-transfer direction in each operating condition. Under the static takeoff-and-landing condition, the battery pack is subjected to a vertical overload of 5 G, and the sandwich core is mainly compressed between the upper and lower enclosure plates. Under the drop-impact condition, an initial velocity of 17.50 m/s is applied along the Y-axis, and the core deformation is dominated by compression along the impact direction. Accordingly, the

homogenized model represents the macroscopic compressive response along the principal loading direction considered in this study, while the complete orthotropic behavior under arbitrary multidirectional loading is not included.

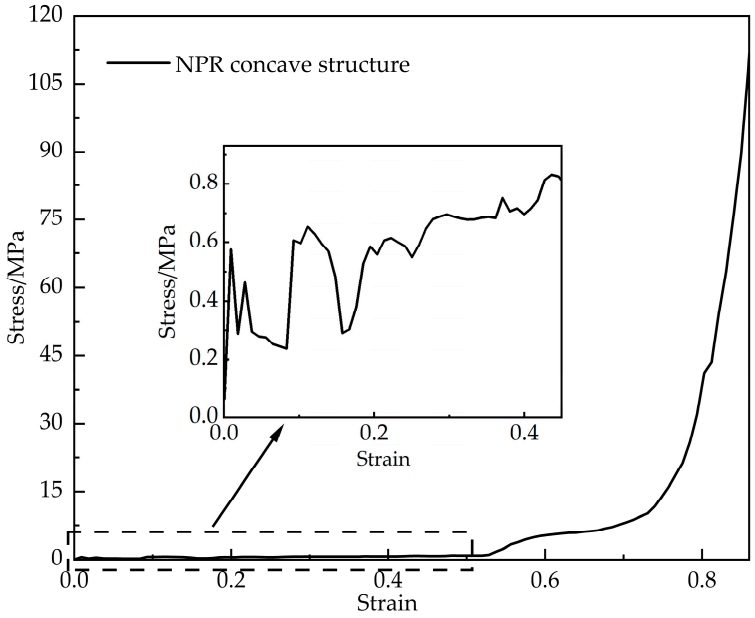


Figure 9. Macroscopic compressive response curve of NPR concave core.

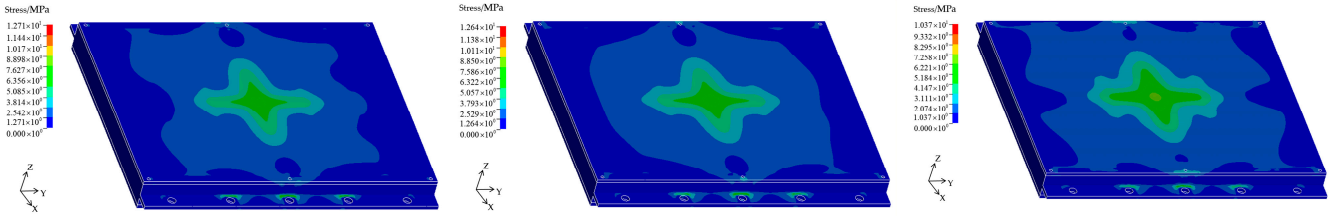
It should also be noted that the tabulated compressive response curve is treated as rate-independent. Therefore, possible strain-rate effects on plateau stress, collapse mode, and densification response are not explicitly captured in the present model. In addition, replacing the explicit cellular geometry with a homogenized continuum inevitably simplifies several local deformation mechanisms, including cell-wall buckling, plastic hinge formation, ligament bending, node rotation, progressive folding, shear-band localization, detailed densification paths, and local interactions between the core and face sheets.

Similar limitations have been reported in homogenized modelling of lattice and cellular materials. Homogenization methods are commonly used to reduce computational cost and predict effective macroscopic properties [42,43], whereas detailed instability, post-buckling deformation, and local collapse mechanisms generally require discrete or explicit cellular models [44]. Therefore, the present homogenized core model is mainly used for the comparative pack-level evaluation of global deformation resistance, load transfer, energy absorption, and intrusion response. It preserves the dominant macroscopic crushing characteristics while improving computational efficiency, but it is not intended to provide detailed prediction of local failure evolution.

4.1. Mesh Independence Analysis

Mesh size in finite element simulations directly affects the ability to capture local stress gradients, as well as the accuracy of the results and computational cost. For battery pack structures involving bolted connections, boundary constraints, and local geometric discontinuities, the maximum stress is usually sensitive to mesh size. Therefore, a mesh-independence analysis is necessary to verify the rationality of the adopted mesh size. Previous studies have shown that mesh quality and mesh density can affect the accuracy and computational efficiency of finite element solutions [31,45]. The key to mesh-independence verification is not to require complete agreement among the results obtained using all mesh sizes, but rather to determine whether the target response quantity tends to stabilize as the mesh is progressively refined [46,47].

To evaluate the mesh sensitivity of the proposed battery pack finite element model, three global mesh sizes, namely 11 mm, 9 mm, and 7 mm, are selected for impact simulations. The impact region is equivalent to a circular area with a diameter of 700 mm acting on the surface of the battery pack, and the peak impact force is set to 30 kN. The 9 mm mesh is adopted as the baseline mesh for the subsequent simulations. The maximum equivalent stresses obtained under different mesh sizes are compared, and the simulation results are shown in Figure 10 and Table 4.



(**a**) (**b**) (**c**)

Figure 10. Stress distributions of the battery pack under different mesh sizes. (**a**) 7 mm. (**b**) 9 mm. (**c**) 11 mm.

Table 4. Comparison of stress with different mesh sizes.

Mesh size/mm	Stress/MPa	Relative Variation Compared with 9 mm/%
7 mm	12.71	0.55
9 mm	12.64	/
11 mm	10.37	17.96

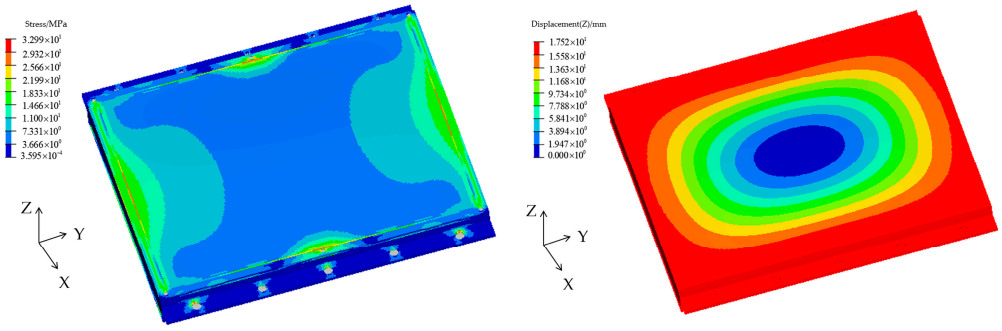
As shown in Table 4, when the mesh size is 11 mm, the maximum stress is 10.37 MPa. When the mesh size is reduced to 9 mm, the maximum stress increased to 12.64 MPa. Taking the 9 mm mesh result as the reference, the relative variation of the 11 mm mesh result is 17.96%. This relatively large difference indicates that the 11 mm coarse mesh cannot sufficiently resolve the stress gradients near the bolted connections, local constraint regions, and structural stiffness discontinuities. As a result, the local peak stress is underestimated. Therefore, the 11 mm mesh has not yet reached a stable mesh convergence state.

When the mesh size is further refined from 9 mm to 7 mm, the maximum stress only changed from 12.64 MPa to 12.71 MPa, with a relative variation of 0.55%. In addition, Figure 10 shows that the locations of the high-stress regions and the overall stress distribution patterns obtained using the 9 mm and 7 mm meshes are basically consistent. According to the grid-refinement and discretization-error assessment studies by Roache [46] and Celik et al. [47], mesh-independence verification should focus on whether the target response quantity tends to stabilize with progressive mesh refinement, rather than requiring complete agreement among all mesh results. In the present study, the difference in maximum stress between the 11 mm and 9 mm meshes is 17.96%, whereas the difference is reduced to only 0.55% when the mesh is further refined from 9 mm to 7 mm. This significant reduction in the difference between adjacent mesh results indicates a clear convergence tendency of the maximum stress response. Therefore, further mesh refinement has only a limited influence on the maximum stress, and the 9 mm mesh can be considered close to the fine-mesh solution and sufficient to satisfy the mesh-independence requirement of the full battery pack finite element model.

4.2. Static Takeoff-and-Landing Operating Condition Analysis

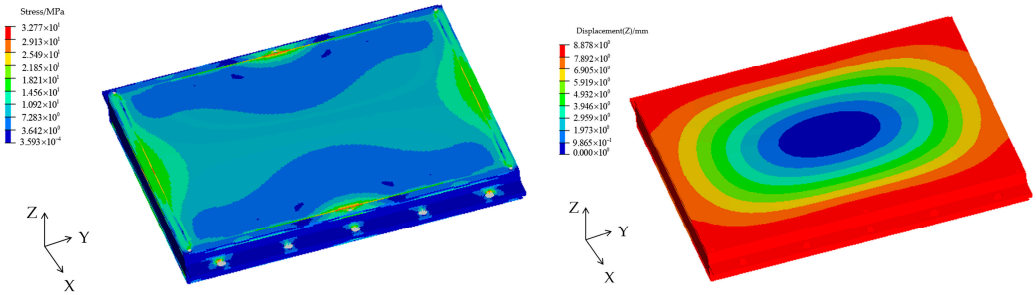
A flying car is subjected to significant vertical inertial loads during takeoff and landing. As a key load-bearing and energy-storage component, the battery pack directly affects

the operational safety of the entire aircraft through its structural stiffness and connection reliability [1,2]. To evaluate the static load-bearing performance of different sandwich structures under takeoff-and-landing conditions, a gravitational acceleration of 5 G is applied to the entire battery pack to represent the equivalent overload at this stage. In addition, Single-point constraints are imposed on translational and rotational degrees of freedom at the lifting-lug bolt locations of the battery pack tray. In the following analysis, the battery pack with a conventional honeycomb sandwich core is referred to as the conventional battery pack, whereas the battery pack with an NPR concave sandwich core is referred to as the novel battery pack. Stress and displacement contours of the conventional battery pack and the novel battery pack under takeoff-and-landing conditions are presented in Figures 11 and 12, respectively.



(**a**) (**b**)

Figure 11. Stress and displacement contours of the conventional battery pack under the static takeoff-and-landing condition. (**a**) Stress contour. (**b**) Displacement contour.



(**a**) (**b**)

Figure 12. Stress and displacement contours of the novel battery pack under the static takeoff-and-landing condition. (**a**) Stress contour. (**b**) Displacement contour.

The results indicate that, under the static takeoff-and-landing condition, battery pack enclosures with conventional honeycomb and NPR concave sandwich structures exhibit similar maximum stress levels, whereas their overall deformation responses differ significantly. Specifically, the maximum equivalent stress of a battery pack enclosure with a conventional honeycomb sandwich core is 32.99 MPa, while that of the enclosure with an NPR concave sandwich core decreases to 32.77 MPa, corresponding to a reduction of 0.67%. Although this reduction is relatively limited, the slightly lower maximum equivalent stress obtained by the NPR concave structure indicates its beneficial contribution to load transfer and local stress regulation. To a certain extent, the vertical load transmission path is optimized, and excessive local stress concentration in specific regions is mitigated.

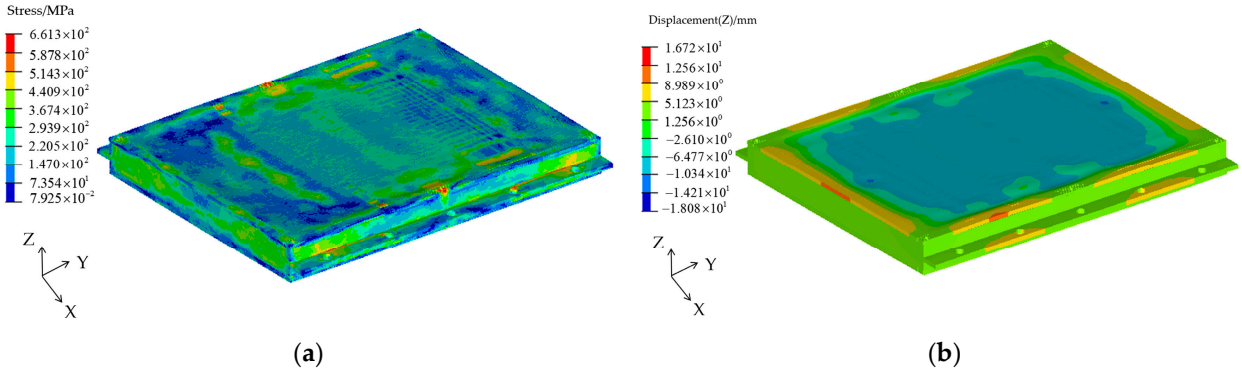
Compared with the stress response, the displacement results more clearly reflect the influence of different sandwich configurations on the overall stiffness and deformation resistance of the battery pack. As described in terms of the displacement contours, the

maximum displacement of a battery pack enclosure with a conventional honeycomb sandwich structure is 17.52 mm, whereas that of the enclosure with an NPR concave structure decreases to 8.88 mm, corresponding to a reduction of 49.31%. This result indicates that the NPR concave structure significantly enhances the overall deformation resistance of battery pack under takeoff-and-landing overload. This improvement is mainly attributed to the higher equivalent supporting stiffness and distinctive lateral contraction mechanism of NPR concave structure. Under vertical loading, the sandwich core enhances overall load-bearing synergy through cell-wall rotation, bending, and inward contraction. Consequently, relative deformation between the upper and lower enclosures is effectively restrained, and overall deflection of battery pack enclosure is reduced.

Overall, under the static takeoff-and-landing condition, NPR concave structure produces only a marginal reduction in the maximum stress of the battery pack. This result indicates that the peak stress in this case is mainly governed by local constraints and the geometric characteristics of the enclosure, whereas the sandwich configuration has only a limited effect. However, while maintaining a nearly identical stress level in the enclosure, the NPR concave sandwich core substantially reduces the overall displacement response of the battery pack, demonstrating superior global stiffness and deformation control capability. Compared with a conventional honeycomb sandwich structure, the NPR concave structure more effectively improves the structural stability of the battery pack under vertical overload during takeoff and landing. Consequently, the risk of excessive deformation adversely affecting the internal battery module and connection regions is reduced.

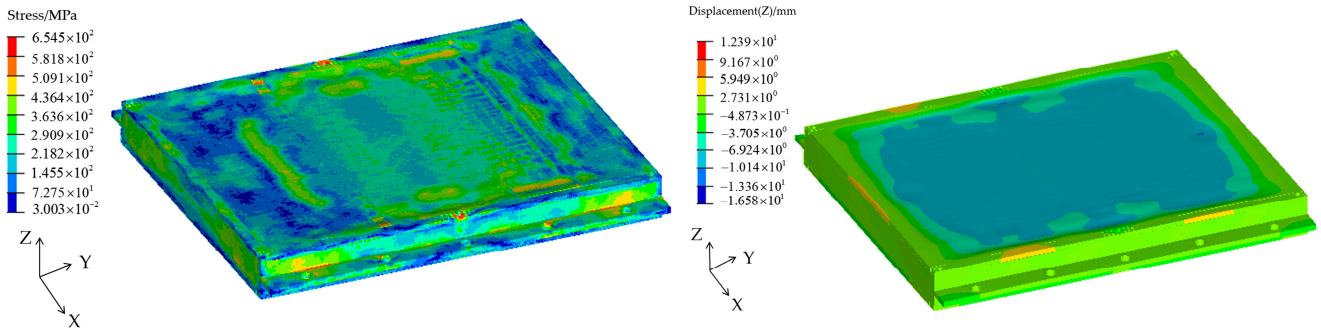
4.3. Dynamic Impact Operating Condition Analysis

During actual flying car operation, the battery pack may be subjected to severe transient impact loads under conditions such as abnormal landing, sudden loss of control, or structural impact [28]. To further evaluate the protective performance of different sandwich structures under dynamic impact conditions, a drop impact simulation of the battery pack is conducted in this study. The drop condition is established with reference to the relevant mechanical safety assessment requirements specified in UN ECE R100 for electric vehicle power battery packs, together with commonly adopted numerical simulation methods for battery pack impact analysis [10,48]. To reduce computational cost, the battery pack is initially positioned 10 mm away from a rigid wall and assigned an initial velocity of 17.50 m/s along the Y-axis, so that impact contact occurs between the battery pack and the rigid wall. Under the flying car drop condition, stress and displacement contours of the conventional battery pack and the novel battery pack are presented in Figures 13 and 14, respectively.



(**a**) (**b**)

Figure 13. Stress and displacement contours of the conventional battery pack under the dynamic drop-impact condition. (**a**) Stress contour. (**b**) Displacement contour.



(**a**) (**b**)

Figure 14. Stress and displacement contours of the novel battery pack under the dynamic drop-impact condition. (**a**) Stress contour. (**b**) Displacement contour.

The results demonstrate that, under the drop condition, conventional and novel battery packs exhibit similar maximum stress levels. High-stress regions are mainly concentrated near bolted connections and local constraint locations. This finding indicates that, during high-speed impact, peak stress is not solely dependent on the sandwich configuration. Instead, it is jointly governed by connection boundary conditions, the equivalent stiffness of bolted joints, and local structural stiffness discontinuities. As bolted connection regions serve as the primary load-transfer paths, local stress concentration is readily generated at the moment of impact. For both sandwich structures, high-stress regions appear near the connection zones, suggesting that the impact load is first transferred through the enclosure and connection structures to the entire battery pack, thereby causing stress concentration in these local regions. Although NPR concave structure does not significantly reduce the overall peak stress, no additional abnormal stress concentration is introduced. This result indicates that the structure can still maintain favorable overall load-bearing stability under dynamic impact.

Compared with the stress response, the intrusion response more clearly reflects the protective differences among the sandwich structures under dynamic impact. According to displacement contours, maximum intrusion of battery pack enclosure with conventional honeycomb sandwich structure is 16.72 mm, whereas that of enclosure with NPR concave structure decreases to 12.39 mm. The intrusion is therefore reduced by 4.33 mm, corresponding to a 25.94% reduction. This result indicates that, under the same impact velocity and boundary conditions, NPR concave structure more effectively suppresses the overall deformation of the battery pack along the impact direction. Meanwhile, the penetration of external impact loads into the internal structure is reduced. This improvement is mainly attributed to cell rotation, cell-wall bending, and the lateral inward contraction of the NPR concave structure during compression. These deformation modes enable the sandwich layer to develop a more coordinated overall deformation pattern in the impact region. The NPR deformation mechanism enhances the ability of the sandwich layer to constrain local impact loads. In addition, the direct transmission of impact loads into the interior of the battery pack is delayed, thereby reducing structural intrusion.

Overall, under the drop condition, the two sandwich structures exhibit no significant difference in maximum stress, and the peak stress is mainly concentrated in local regions such as the bolted connections. This indicates that, under this condition, the maximum stress is governed primarily by the connection boundaries and local structural features, whereas the influence of the sandwich configuration remains limited. However, the NPR concave structure significantly reduces the maximum intrusion of the battery pack, demonstrating superior anti-intrusion performance and deformation control capability. Compared with a conventional honeycomb sandwich structure, the NPR concave structure more

effectively improves the displacement response of the battery pack under impact loading without introducing any obvious additional stress concentration. These results suggest that it provides greater benefits for enhancing the structural protection performance of the flying car power battery pack under dynamic drop conditions.

It should be noted that the present dynamic impact simulations are conducted using rate-independent constitutive models for the shell materials and the homogenized core response. Therefore, the obtained results are mainly used for the comparative evaluation of deformation resistance and anti-intrusion capability under identical material assumptions. The possible influence of strain-rate-dependent material behavior on peak stress, crushing force, and local failure evolution will be further investigated in future work.

5. Conclusions

A tortoise-carapace-inspired metamaterial sandwich structure is proposed for flying car power battery pack protection. Firstly, a biomimetic sandwich structure is established based on the hierarchical protective mechanism of tortoise carapace. The proposed structure consists of an outer shell, a sandwich core, and an inner shell. Subsequently, three sandwich core configurations are designed, namely conventional honeycomb, NPR chiral structure, and NPR concave structure. Their deformation and failure behaviors, energy absorption characteristics, and anti-intrusion performance are compared under high-speed impact conditions. Based on the comparison results, the optimal sandwich core configuration for the flying car power battery pack is identified. Finally, finite element simulations are conducted for the conventional battery pack and proposed battery pack under typical static takeoff-and-landing conditions, as well as the dynamic drop conditions of a flying car. The results demonstrate that the proposed design achieves enhanced structural stiffness, deformation resistance, and impact protection performance. The main conclusions are summarized as follows:

(1) Based on the hierarchical protective structure of a tortoise carapace, a biomimetic sandwich structure model is established for the flying car power battery pack. The structural characteristics of the tortoise carapace is translated into the battery pack design. Consequently, when the battery pack enclosure is subjected to external loads, load diffusion, deformation buffering, and energy dissipation are achieved through the synergistic action of the multilayer structure, thereby enhancing the protection of the internal battery module.

(2) By comparing the impact performance of the conventional honeycomb, an NPR chiral structure, and an NPR concave structure, the NPR concave structure is selected as the preferred core configuration based on a comprehensive trade-off among energy absorption, peak load control, crushing stability, and deformation resistance. Although the SEA of the NPR concave structure is lower than that of the NPR chiral structure, it remains higher than that of the conventional honeycomb and provides more favorable peak load control and deformation stability. Therefore, the NPR concave structure is more suitable for the design objective of improving pack-level deformation resistance and anti-intrusion capability as its SEA reaches 1.31 kJ/kg. Although this value is lower than that of the NPR chiral structure, which reaches 3.14 kJ/kg, it remains significantly higher than that of the conventional honeycomb, which is 0.56 kJ/kg. Meanwhile, its PCF is 43.38 kN, which is lower than that of the conventional honeycomb but higher than that of the NPR chiral structure. These results indicate that NPR concave structure offers distinct advantages in energy absorption efficiency, peak load control, and crushing stability. Therefore, it is selected as the optimal core configuration for the sandwich structure of the flying car power battery pack.

(3) In the operating condition analysis, the proposed battery pack demonstrates enhanced overall protective performance. Under the static takeoff-and-landing condition, the maximum displacement of the battery pack enclosure decreases from 17.52 mm to 8.88 mm, corresponding to a reduction of 49.31%. Under the dynamic drop condition, the maximum intrusion decreases from 16.72 mm to 12.39 mm, corresponding to a reduction of 25.94%. These results demonstrate that the NPR concave structure effectively enhances the overall deformation resistance and anti-intrusion capability of the battery pack. Therefore, the structural safety of a flying car power battery pack under complex operating conditions is enhanced.

Author Contributions: Conceptualization, Y.Z. and Y.W. (Yueqiang Wang); methodology, Y.Z.; software, K.C.; validation, K.C. and X.S.; formal analysis, K.C.; investigation, B.Z.; resources, Y.Z. and Y.W. (Yueqiang Wang); data curation, J.H.; writing—original draft preparation, K.C.; writing—review and editing, Y.Z., Y.W. (Yueqiang Wang) and Y.W. (Yangwei Wang); supervision, Y.Z., Y.W. (Yueqiang Wang) and Y.W. (Yangwei Wang); project administration, Y.Z. and Y.W. (Yueqiang Wang); funding acquisition, Y.Z. All authors have read and agreed to the published version of the manuscript.

Funding: This research is funded by National Key Laboratory Foundation of Science and Technology on Materials under Shock and Impact (grant number WDZC2024-7), the New Chongqing Youth Innovation Talent Project (grant number CSTB2024NSCQ-QCXMX0038), the Fundamental Research Funds for the Central Universities (grant number SWU-KT26054), and the Natural Science Foundation of Chongqing (grant number CSTB2024NSCQ-MSX0954). The authors gratefully acknowledge the help and support received from Zhao's Team. Most importantly, the authors are very grateful to the editors and all of the anonymous referees for their constructive comments.

Data Availability Statement: The original contributions presented in this study are included in the article. Further inquiries can be directed to the corresponding author.

Conflicts of Interest: The authors declare no conflicts of interest.

Abbreviations

The following abbreviations are used in this manuscript:

NPR	Negative Poisson's ratio
PCF	Peak crushing force
SEA	Specific energy absorption

References

1. Laarmann, L.; Thoma, A.; Misch, P.; Röth, T.; Braun, C.; Watkins, S.; Fard, M. Automotive safety approach for future eVTOL vehicles. *CEAS Aeronaut. J.* **2023**, *14*, 369–379. [CrossRef]
2. Wadia, K.; Buszek, M.; Poliakov, N.; Castro, S.G. Preliminary design and analysis of crashworthy structures for a long-range eVTOL aircraft. In Proceedings of the AIAA SCITECH 2022 Forum, San Diego, CA, USA, 3–7 January 2022. [CrossRef]
3. Feng, X.; Ouyang, M.; Liu, X.; Lu, L.; Xia, Y.; He, X. Thermal runaway mechanism of lithium ion battery for electric vehicles: A review. *Energy Storage Mater.* **2018**, *10*, 246–267. [CrossRef]
4. Arora, S.; Shen, W.; Kapoor, A. Review of mechanical design and strategic placement technique of a robust battery pack for electric vehicles. *Renew. Sustain. Energy Rev.* **2016**, *60*, 1319–1331. [CrossRef]
5. Wang, Q.; Ping, P.; Zhao, X.; Chu, G.; Sun, J.; Chen, C. Thermal runaway caused fire and explosion of lithium ion battery. *J. Power Sources* **2012**, *208*, 210–224. [CrossRef]
6. United Nations Economic Commission for Europe. *UN Regulation No. 66: Uniform Technical Prescriptions Concerning the Approval of Large Passenger Vehicles with Regard to the Strength of Their Superstructure*; UNECE: Geneva, Switzerland, 2006.
7. Karliński, J.; Ptak, M.; Działak, P.; Rusiński, E. Strength analysis of bus superstructure according to Regulation No. 66 of UN/ECE. *Arch. Civ. Mech. Eng.* **2014**, *14*, 342–353. [CrossRef]
8. Liang, C.C.; Le, G.N. Analysis of bus rollover protection under legislated standards using LS-DYNA software simulation techniques. *Int. J. Automot. Technol.* **2010**, *11*, 495–506. [CrossRef]

9. Kunakorn-ong, P.; Jongpradist, P. Optimisation of bus superstructure for rollover safety according to ECE-R66. *Int. J. Automot. Technol.* **2020**, *21*, 215–225. [CrossRef]
10. United Nations Economic Commission for Europe. *UN Regulation No. 100: Uniform Provisions Concerning the Approval of Vehicles with Regard to Specific Requirements for the Electric Power Train*; UNECE: Geneva, Switzerland, 2016.
11. Sordi, A.; Menino, B.G.; Isoton Pistorello, G.; do Nascimento, V.; Telli, G.D. Performance of electric bus batteries in rollover scenarios according to ECE R66 and R100 standards. *World Electr. Veh. J.* **2025**, *16*, 528. [CrossRef]
12. Pan, Y.; Xiong, Y.; Dai, W.; Diao, K.; Wu, L.; Wang, J. Crush and crash analysis of an automotive battery pack enclosure for lightweight design. *Int. J. Crashworthiness* **2022**, *27*, 368–387. [CrossRef]
13. Agarwal, A.; Batista, R.C.; Tashi. Crashworthiness evaluation of electric vehicle battery pack using honeycombs and explicit dynamic analysis. *E3S Web Conf.* **2024**, *519*, 04010. [CrossRef]
14. Wegst, U.G.K.; Bai, H.; Saiz, E.; Tomsia, A.P.; Ritchie, R.O. Bioinspired structural materials. *Nat. Mater.* **2015**, *14*, 23–36. [CrossRef] [PubMed]
15. Liu, K.; Jiang, L. Bio-inspired design of multiscale structures for function integration. *Nano Today* **2011**, *6*, 155–175. [CrossRef]
16. Lazarus, B.S.; Velasco-Hogan, A.; Río, T.G.-D.; Meyers, M.A.; Jasiuk, I. A review of impact resistant biological and bioinspired materials and structures. *J. Mater. Res. Technol.* **2020**, *9*, 15789–15824. [CrossRef]
17. Patadiya, J.; Wang, X.; Joshi, G.; Kandasubramanian, B.; Naebe, M. 3D-printed biomimetic hierarchical nacre architecture: Fracture behavior and analysis. *ACS Omega* **2023**, *8*, 18544–18556. [CrossRef] [PubMed]
18. Bejan, A.; Lorente, S. Constructal theory of generation of configuration in nature and engineering. *J. Appl. Phys.* **2006**, *100*, 041301. [CrossRef]
19. Reis, A.H. Constructal theory: From engineering to physics, and how flow systems develop shape and structure. *Appl. Mech. Rev.* **2006**, *59*, 269–282. [CrossRef]
20. Bejan, A.; Lorente, S. The constructal law of design and evolution in nature. *Philos. Trans. R. Soc. B Biol. Sci.* **2010**, *365*, 1335–1347. [CrossRef] [PubMed]
21. Rhee, H.; Horstemeyer, M.F.; Hwang, Y.; Lim, H.; El Kadiri, H.; Trim, W. A study on the structure and mechanical behavior of the Terrapene carolina carapace: A pathway to design bio-inspired synthetic composites. *Mater. Sci. Eng. C* **2009**, *29*, 2333–2339. [CrossRef]
22. Pei, B.; Guo, L.; Wu, M.; Hu, S.; Wu, Y.; Wang, Y. Impact resistant structure design and optimization inspired by turtle carapace. *Materials* **2022**, *15*, 2899. [CrossRef] [PubMed]
23. Surjadi, J.U.; Gao, L.; Du, H.; Li, X.; Xiong, X.; Fang, N.X.; Lu, Y. Mechanical metamaterials and their engineering applications. *Adv. Eng. Mater.* **2019**, *21*, 1800864. [CrossRef]
24. Du, F.; Jin, Z.; Yang, R.; Hao, M.; Wang, J.; Xu, G.; Zuo, W.; Geng, Z.; Pan, H.; Li, T.; et al. Thermally insulating and fire-retardant bio-mimic structural composites with a negative Poisson's ratio for battery protection. *Carbon Energy* **2023**, *5*, e353. [CrossRef]
25. Jiang, H.; Ren, Y.; Gao, B.; Guo, X. Insight into the negative Poisson's ratio effect of metallic auxetic reentrant honeycomb under dynamic compression. *Mater. Sci. Eng. A* **2019**, *750*, 138–151. [CrossRef]
26. Scurtu, I.L.; Szabo, I.; Gheres, M. Numerical analysis of crashworthiness on electric vehicle's battery case with auxetic structure. *Energies* **2023**, *16*, 5849. [CrossRef]
27. Biharta, M.A.S.; Santosa, S.P.; Widagdo, D. Design and optimization of lithium-ion battery protector with auxetic honeycomb for in-plane impact using machine learning method. *Front. Energy Res.* **2023**, *11*, 1114263. [CrossRef]
28. Littell, J.; Gardner, N.; Ellafrits, S. Dynamic drop testing of eVTOL energy storage systems Part 2: Deformation and post-test forensics results. In Proceedings of the Vertical Flight Society's 81st Annual Forum & Technology Display, Virginia Beach, VA, USA, 20–22 May 2025. [CrossRef]
29. Sahraei, E.; Hill, R.; Wierzbicki, T. Calibration and finite element simulation of pouch lithium-ion batteries for mechanical integrity. *J. Power Sources* **2012**, *201*, 307–321. [CrossRef]
30. Greve, L.; Fehrenbach, C. Mechanical testing and macro-mechanical finite element simulation of the deformation, fracture, and short circuit initiation of cylindrical lithium ion battery cells. *J. Power Sources* **2012**, *214*, 377–385. [CrossRef]
31. Vartziotis, D.; Wipper, J.; Papadrakakis, M. Improving mesh quality and finite element solution accuracy by GETMe smoothing in solving the Poisson equation. *Finite Elem. Anal. Des.* **2013**, *66*, 36–52. [CrossRef]
32. Masters, I.G.; Evans, K.E. Models for the elastic deformation of honeycombs. *Compos. Struct.* **1996**, *35*, 403–422. [CrossRef]
33. Gibson, L.J.; Ashby, M.F. The mechanics of three-dimensional cellular materials. *Proc. R. Soc. A* **1982**, *382*, 43–59. [CrossRef]
34. Prall, D.; Lakes, R.S. Properties of a chiral honeycomb with a Poisson's ratio of −1. *Int. J. Mech. Sci.* **1997**, *39*, 305–314. [CrossRef]
35. Spadoni, A.; Ruzzene, M.; Gonella, S.; Scarpa, F. Phononic properties of hexagonal chiral lattices. *Wave Motion* **2009**, *46*, 435–450. [CrossRef]
36. Lakes, R. Foam structures with a negative Poisson's ratio. *Science* **1987**, *235*, 1038–1040. [CrossRef] [PubMed]
37. Ruan, D.; Lu, G.; Wang, B.; Yu, T.X. In-plane dynamic crushing of honeycombs—A finite element study. *Int. J. Impact Eng.* **2003**, *28*, 161–182. [CrossRef]

38. Dong, Z.; Li, Y.; Zhao, T.; Wu, W.; Xiao, D.; Liang, J. Experimental and numerical studies on the compressive mechanical properties of the metallic auxetic reentrant honeycomb. *Mater. Des.* **2019**, *182*, 108036. [CrossRef]
39. Gao, D.; Zhang, J.; Zhang, C.; You, Y. Dynamic compressive and flexural behaviour of re-entrant auxetics: A numerical study. *Materials* **2023**, *16*, 5219. [CrossRef] [PubMed]
40. Qi, D.; Lu, Q.; He, C.; Li, Y.; Wu, W.; Xiao, D. Impact energy absorption of functionally graded chiral honeycomb structures. *Extrem. Mech. Lett.* **2019**, *32*, 100568. [CrossRef]
41. Shen, L.; Wang, Z.; Wang, X.; Wei, K. Negative Poisson's ratio and effective Young's modulus of a vertex-based hierarchical re-entrant honeycomb. *Int. J. Mech. Sci.* **2021**, *206*, 106611. [CrossRef]
42. Arabnejad, S.; Pasini, D. Mechanical properties of lattice materials via asymptotic homogenization and comparison with alternative homogenization methods. *Int. J. Mech. Sci.* **2013**, *77*, 249–262. [CrossRef]
43. Somnic, J.; Jo, B.W. Status and challenges in homogenization methods for lattice materials. *Materials* **2022**, *15*, 605. [CrossRef] [PubMed]
44. Völlmecke, C.; Todt, M.; Yiatros, S. Buckling and postbuckling of architectured materials: A review of methods for lattice structures and metal foams. *Compos. Adv. Mater.* **2021**, *30*, 26349833211003904. [CrossRef]
45. Pisarciuc, C.; Dan, I.; Cioară, R. The Influence of Mesh Density on the Results Obtained by Finite Element Analysis of Complex Bodies. *Materials* **2023**, *16*, 2555. [CrossRef] [PubMed]
46. Roache, P.J. Perspective: A Method for Uniform Reporting of Grid Refinement Studies. *J. Fluids Eng.* **1994**, *116*, 405–413. [CrossRef]
47. Celik, I.B.; Ghia, U.; Roache, P.J.; Freitas, C.J.; Coleman, H.; Raad, P.E. Procedure for Estimation and Reporting of Uncertainty Due to Discretization in CFD Applications. *J. Fluids Eng.* **2008**, *130*, 078001. [CrossRef]
48. Arslan, M.; Karamangil, M.İ. Comprehensive optimization and design of an electric vehicle battery box side profile for lightweight and crashworthiness using a novel hybrid structure. *Appl. Sci.* **2025**, *15*, 2037. [CrossRef]

Disclaimer/Publisher's Note: The statements, opinions and data contained in all publications are solely those of the individual author(s) and contributor(s) and not of MDPI and/or the editor(s). MDPI and/or the editor(s) disclaim responsibility for any injury to people or property resulting from any ideas, methods, instructions or products referred to in the content.